Article:
Kim, E-J and Hollerbach, R orcid.org/0000-0001-8639-0967 (2023) A stochastic model of edge-localized modes in magnetically confined plasmas. Philosophical Transactions of the Royal Society A: Mathematical, Physical and Engineering Sciences, 381 (2242). 20210226. ISSN 1364-503X

https://doi.org/10.1098/rsta.2021.0226

A Stochastic Model of Edge-localised Modes in Magnetically Confined Plasmas

Eun-jin Kim[1] and Rainer Hollerbach[2]

[1]Fluid and Complex System Research Centre, Coventry University, Coventry CV1 2TT, UK

[2]Department of Applied Mathematics, University of Leeds, Leeds LS2 9JT, UK

Abstract

Magnetically confined plasmas are far from equilibrium and pose considerable challenges in statistical analysis. We discuss a non-perturbative statistical method, namely a time-dependent density function (PDF) approach that is potentially useful for analysing time-varying, large, or non-Gaussian fluctuations and bursty events associated with instabilities in the L-H transition and the H-mode. Specifically, we present a stochastic Langevin model of edge-localised modes (ELMs) by including stochastic noise terms in a previous ODE ELM model. We calculate exact time-dependent PDFs by numerically solving the Fokker-Planck equation and characterise time-varying statistical properties of ELMs for different energy fluxes and noise amplitudes. The stochastic noise is shown to introduce phase-mixing and plays a significant role in mitigating extreme bursts of large ELMs. Furthermore, based on time-dependent PDFs, we provide a path-dependent information geometric theory of the ELM dynamics and demonstrate its utility in capturing self-regulatory relaxation oscillations, bursts, and a sudden change in the system.

1. Introduction

Magnetically confined plasmas constitute one of the important examples of complex systems operating far from equilibrium[1]. Despite the complexity, self-regulatory behaviour often emerges spontaneously[2, 3, 4] and plays a vital role in plasma confinement. For instance, when the input power exceeds a critical power threshold, the transition from a low-confinement mode (L-mode) to a high-confinement mode (H-mode) can occur spontaneously, where plasmas organise themselves into an 'ordered', high-confinement state [5, 6, 7, 8, 9, 10, 11, 12, 13, 14, 15, 16, 17, 18, 19, 20]. occur spontaneously, where plasmas organise themselves into an 'ordered', high-confinement state [5, 6, 7, 8, 9, 10, 11, 12, 13, 14, 15, 16, 17, 18, 19, 20]. Reproduced in different fusion devices (tokamaks, stellarators, reversed field pinch) since the first discovery in 1980s[5], the Low-to-High confinement (L-H) transition is now believed to be triggered by the spontaneous formation of $\mathbf{E} \times \mathbf{B}$ macro/meso scale shear flows (mean shear/zonal flows) which significantly reduce the transport via turbulence suppression by shear flows[21, 22, 23, 24, 25]. In particular, zonal flows generated from small-scale turbulence in turn regulate turbulence by shearing, leading to self-regulatory oscillations (called dithering)[14, 15, 16, 17, 18, 19, 20, 26, 27, 28].

The H-mode being a baseline scenario for ITER [13, 20, 26, 29], it remains important to improve our understanding of threshold power scaling, the effects of density, magnetic geometry and neutrals, triggering mechanisms and causality relations, hysteresis, etc. [13]. For instance, to elucidate the self-regulation between zonal flows and turbulence, bicoherence spectral analysis, phase space portrait, Reynolds stress analysis, etc. are employed.

A stochastic model of the L-H transition[30, 31] was recently proposed to provide an alternative, non-perturbative method of characterising statistical properties and self-regulation (see §1.1..2 below for details).

The key characteristic of the H-mode is the formation of a shear layer and a steep gradient of the edge plasma pressure profile. The latter can become unstable for a sufficiently large input power and cause relaxation-type oscillations – the so-called edge-localised modes (ELMs)[32, 33, 34, 35, 36] – as the pressure gradient hovers around its critical value through self-regulation. The resulting quasi-periodic oscillations degrade confinement, potentially causing significant damages. This highlights the importance of ELM mitigation, e.g. by resonant magnetic perturbations or pellet injection in DIII-D and ASDEX-U tokamaks[35, 36]. It is also vital to accurately characterise the statistical properties of ELM dynamics to elucidate the interaction among different players, in particular, self-regulatory behaviour or large bursts. The aim of this paper is to propose a stochastic ELM model and present new methods that will enable us to address these issues. These involve a time-dependent Probability Density Function (PDF) method and information geometric theory[37]. As a motivation for our method, we discuss the limitations of perturbative methods in §1.1..1 and the essence of our methods in §1.1..2 below.

1..1 Perturbative methods

Near equilibrium, fluctuations are weak and satisfy Gaussian statistics, validating perturbative methods. For instance, the Reynolds stress, defined by the second moment of the different components of the fluctuating velocity, quantifies the amount of the energy exchange between the mean velocity and fluctuating parts. It can quantify energy extracted from small scales to form a large-scale flow (such as zonal flows), and the ratio of the Reynolds stress to the energy input into turbulence (normalised Reynolds power [38]) was used as a criterion of the L-H transition.

However, far from equilibrium or for anomalous transport/bursty events, a PDF is no longer Gaussian. Some examples would be a negatively or positively skewed PDF with an elevated left or right tail, e.g., associated with rare, but large-amplitude events where the mean value is smaller or larger than the peak position, respectively. Furthermore, a PDF can have more than one peak such as a bimodal PDF. For a symmetric bimodal PDF, the mean value occurs at the local minimum and has nothing to do with the most likely value. To appreciate the significance of this, let us imagine the case where PDF peaks represent (different) coherent structures for both symmetric bimodal PDF and unimodal PDF that have the same mean value. Then, for a unimodal case, the mean value represents a coherent structure, and the energy transfer between fluctuations and the structure is quantified by the Reynolds stress in the usual way. However, for a bimodal PDF where its two peaks represent coherent structures (e.g., vortex-pairs), fluctuations should be measured with respect to these coherent structures (not the deviation from the mean value) for the Reynolds stress to be physically meaningful. In general, PDFs may be asymmetric, bimodal, or multimodal.

1..2 PDF method and path-dependent statistical diagnostics

To overcome the limitations of perturbative methods noted in §1.1..1, it is advantageous to deal with a PDF itself, say for a variable x. Here, x can be density fluctuation, electric potential, zonal flows, pressure gradient, or magnetic fluctuations. For more than one variable, say x and y, we will consider a joint PDF $p(x, y, t)$ which depends on time t that is useful

for describing large fluctuations or time-varying statistical properties.

It is important to note that for given PDFs $p(x, t_0)$ and $p(x, t_F)$ at time t_0 and t_F ($> t_0$), there is an infinite number of different evolution paths that connect these two PDFs. For instance, when $p(x, t_0)$ and $p(x, t_F)$ represent PDFs before and after the L-H transition or ELM burst, we are interested in how $p(x, t_0)$ evolves to $p(x, t_F)$[39]. Experimentally, the determination of a PDF would require high-quality statistical samples (over time or space), which would benefit from improved diagnostics and resolutions. To gain a key insight, it is always useful to investigate theoretical and computational models to calculate time-dependent PDFs exactly.

Once we have a time-dependent PDF, we can then look at how various statistical diagnostics change along the trajectory. In this paper, we utilise the information geometry that refers to the application of differential geometry to probability and statistics [37, 40, 41, 42]. This is a powerful tool for elucidating the disparity between different probabilities as well as for linking complexity and geometry (e.g., see [37, 40] and references therein). Our focus will be on the path-dependent information geometric concept (information length and rate) that quantifies the time evolution of a system in terms of a dimensionless distance in a statistical space [37, 43, 44, 45, 46, 47, 48, 30, 31] or the change in information. Their key properties are summarised in Section 2..

1..3 Aims of this paper and outlook

The aim of this paper is to present a stochastic model of ELMs and the analysis of time-dependent PDFs and path-dependent information geometry. The remainder of this paper is organised as follows. We recall our path-dependent information geometric theory in §2. and put forward our stochastic ELM model in Section 3.. Section 4. describes our numerical methods. Sections 5. and 6. provide results and discussions/conclusion, respectively.

2. Path-dependent information geometric diagnostics

Using time-dependent PDFs, we will investigate the path-dependent information geometry by quantifying the change in a PDF by a distance along the evolution path. For instance, for a time-dependent PDF $p(x, t)$, we measure the change in statistical states of x by calculating the information rate Γ from an infinitesimal symmetric relative entropy between $p(x, t)$ and $p(x, t + \delta t)$ as $\delta t \to 0$, and then calculate (dimensionless) information length $\mathcal{L}(t)$ by integrating Γ over time as follows [37, 44, 45, 46, 47, 48, 49]:

$$\Gamma(t)^2 = \int dx \frac{1}{p(x,t)} \left[\frac{\partial p(x,t)}{\partial t}\right]^2, \qquad \mathcal{L}(t) = \int_0^t dt_1 \Gamma(t_1). \tag{1}$$

The unit of Γ^{-1} in Eq. (1) is time, representing a dynamical time unit for information change or the rate of change in information. The faster the temporal change in a PDF is, the larger the information rate is. $\mathcal{L}(t)$ can be interpreted as the total clock time measured in units of Γ^{-1}, and equivalently as the total number of statistically different states that x passes through between time 0 and t. By definition, $\mathcal{L}(t) = 0$ at $t = 0$. In simple terms, $\mathcal{L}(t)$ quantifies the cumulative change in $p(x, t)$ accounting for the uncertainty in measuring x due to a finite width of $p(x, t)$.

To understand what this means, let us consider a Gaussian PDF, which is completely determined by the two parameters $\lambda^i = (\mu, \sigma)$, where μ and σ are the mean value and

standard deviation, respectively, and express Γ as follows:

$$\Gamma^2 = g_{ij}\partial_t\lambda^i\partial_t\lambda^j. \tag{2}$$

Here, g_{ij} is the metric tensor defined in the statistical space spanned by the parameters λ^i as

$$g_{ij}(t) = \int dx p(x,t)(\partial_{\lambda^i}\ln p)\,(\partial_{\lambda^j}\ln p) = \frac{1}{\sigma^2}\begin{pmatrix}1 & 0\\ 0 & 2\end{pmatrix}. \tag{3}$$

Note that g_{ij} has only non-zero diagonal components, with a factor of the variance σ^2 in the denominator. Consequently, a broad PDF with large σ tends to make $\Gamma(t)$ and $\mathcal{L}(t)$ smaller. For constant σ, Eq. (2) is simplified as

$$\Gamma(t) = \left|\frac{1}{\sigma}\frac{d\mu}{dt}\right|. \tag{4}$$

Thus, $\Gamma(t)$ measures how quickly the mean value normalised by the constant σ changes with time. If $\mu > 0$ monotonically decreases over time, Eq. (4) gives $\mathcal{L}(t) = \frac{\mu(t)-\mu(t=0)}{\sigma}$, which is the total change in the mean value divided by the constant σ. Since σ provides the uncertainty in x, $\mathcal{L}(t)$ signifies the change in the physical distance normalised by its uncertainty. However, even when $\mu(t=0) = \mu(t=t_F) = a > 0$, $\mathcal{L}(t_F)$ does not necessarily vanish. For instance, when $\min(\mu(t)) = 0$ at the intermediate time $0 < t < t_F$, $\mathcal{L}(t) = \frac{2a}{\sigma} > 0$ despite the same initial and final PDF with zero total change in μ ($\mu(t_F) - \mu(0) = 0$) due to $\mathcal{L}$'s path-dependence.

For a joint PDF $p(x,y,t)$ for the two variables x and y, Eq. (1) can be extended as

$$\mathcal{L}(t) = \int_0^t dt_1\Gamma(t_1), \qquad \Gamma(t)^2 = \int dxdy\frac{1}{p(x,y,t)}\left[\frac{\partial p(x,y,t)}{\partial t}\right]^2. \tag{5}$$

On the other hand, from the marginal PDFs $p(x,t) = \int dy\, p(x,y,t)$ and $p(y,t) = \int dx\, p(x,y,t)$, we define

$$\mathcal{L}_x(t) = \int_0^t dt_1\Gamma_x(t_1), \qquad \mathcal{L}_y(t) = \int_0^t dt_1\Gamma_y(t_1), \tag{6}$$

$$\Gamma_x(t)^2 = \int dx\frac{1}{p(x,t)}\left[\frac{\partial p(x,t)}{\partial t}\right]^2, \qquad \Gamma_y(t)^2 = \int dy\frac{1}{p(y,t)}\left[\frac{\partial p(y,t)}{\partial t}\right]^2. \tag{7}$$

Γ and $\mathcal{L}$ are *invariant under (time-independent) change of variables*, and thus can be directly compared with each other unlike physical variables having different units. This enables us to compare the time-evolution of $\mathcal{L}_x$ and $\mathcal{L}_y$ or Γ_x and Γ_y of different variables x and y to understand their correlation [47, 30, 31, 37, 43]. For instance, a strong correlation between two interacting species (via random switching) was captured by the same evolution of $\mathcal{L}(t)$ of the two [47]; the self-regulation between turbulence and zonal flows during dithering in the L-H transition was demonstrated by the competition and regulation between their Γ's [30, 31]. Furthermore, the path-dependence is desirable for measuring hysteresis involved in phase transitions [44] such as the L-H transition[30, 31] since a non-equilibrium time-evolution does not obey time-symmetry (time-irreversibility) even when an external force is symmetric in time.

3. Model

In this section, we recall the deterministic toy ODE model of ELMs in §3.3..1 and then provide its stochastic extension in §3.3..2.

3..1 ODE ELM Model

We consider the deterministic ODE model of ELMs[32] where the electric field resulting from the radial force balance on ions is mainly driven by the pressure gradient P, with a negligible contribution from the poloidal velocity. This corresponds to the limit where the diamagnetic velocity is much larger than the poloidal velocity for the input power P_{in} far above the critical power-threshold P_{cr} (see [32]). The reason for focusing on this limit was to reduce computational times for high-resolution runs.

In this limit, the evolution of the pressure gradient P and magnetic fluctuation amplitude E_M is given by[32]

$$\frac{dP}{dt} = \Phi - \tilde{D}(P)P - E_M P, \tag{8}$$

$$\frac{dE_M}{dt} = \lambda(P-1)E_M, \tag{9}$$

$$\tilde{D} = d_0 + d(P - c^2P^4)\Theta(\tilde{P} - P). \tag{10}$$

Here, $\Theta(x)$ is the Heaviside function with $\Theta(x) = 1$ for $x \geq 0$ and $\Theta(x) = 0$ for $x < 0$; $\tilde{P}$ is the critical pressure gradient P for the complete suppression of turbulence due to the shear; $c \equiv \tilde{P}^{-3/2}$. Φ is the control parameter, proportional to the incoming particle flux and represents the energy flux to the system under the assumption of a constant temperature. λ and $d_0 \ll d$ are non-negative constants. Eqs. (8)-(10) are non-dimensionalised such that time t is in the units of $[(c_s/\rho_s)k\rho_s(\Delta_c^4/\rho_s^2L_p^2)]^{-1}$ where $c_s = \sqrt{T_e/m_i}$ is the ion sound speed, $\rho_s = c_s/\omega_{ci}$, ω_{ci} is the ion cyclotron frequency, and k and Δ_c are the poloidal wave number and radial correlation length of the turbulence (see [32] for details).[1]

Due to the lack of a contribution from the poloidal flow to $E \times B$ shear flows, the system supports a direct transition from the L-mode into the ELM H mode (without an ELM-free H-mode gap). While different types of solutions exist depending on $\tilde{P}$ and Φ[32], here we focus on the H-mode state with MHD activity ($E_M \neq 0$) for $1 < \tilde{P} \leq \left(\frac{5}{2}\right)^{1/3}$, $\Phi > [d_0 + \left(\frac{2}{5}\right)^{4/3}\tilde{P}d]\left(\frac{2}{5}\right)^{1/3}\tilde{P}$, and $d_0 \ll d$ to demonstrate how our methods work.

Figure 1 shows the time-evolution of $x = P$ and $y = \sqrt{E_M}$ in Eqs. (8)-(10). Since the period of ELMs decreases with increasing Φ, larger t values are used for smaller Φ. For $\frac{\Phi}{d} = 0.4$, x and y exhibit giant ELMs with a long period and a short duration of magnetic activity where $y \neq 0$.[2] These giant ELMs turn into smaller (so-called grassy) ELMs as $\frac{\Phi}{d}$ is increased, the period becoming smaller while the time duration of magnetic activity increases. The latter two become comparable for $\frac{\Phi}{d} = 1.2$. It is also worth noting that for $\frac{\Phi}{d} = 0.4$, x and y stay mostly around the unstable L-mode solution ($x < 1, y = 0$) while

[1] Obviously, parameter values depend on the characteristics of plasmas and turbulence. For MAST edge plasmas [50] with $B \sim 0.5$ T, $T_e \sim 50$ eV, $\rho_s \sim 0.5$ cm, $\Delta_c \sim 1$ cm, and $L_p \sim (1-10)\rho_s$ the time unit is $\sim (1-30)\mu$secs. For DIII-D edge plasmas with $B \sim 2$ T, $T_e \sim 200$ eV, $\rho_s \sim 0.2$ cm, $k\rho_s \sim 0.1$, $\Delta_c \sim (5-10)\rho_s$[51], and $L_p \sim 5$ cm, the time unit is $O(1-10)\mu$secs.

[2] Using that our time unit is of $O(1-10)$ μsecs, the ELMs in Figure 1 can be seen to have frequencies of order $1-100$ KHz.

making occasional excursions in large bursts. For larger $\frac{\Phi}{d} = 0.8$ and 1.2, the oscillations occur more symmetrically around $x = 1$ (ballooning instability boundary). These features will also be seen in PDFs as discussed later (see the discussion about Figures 3-4 below).

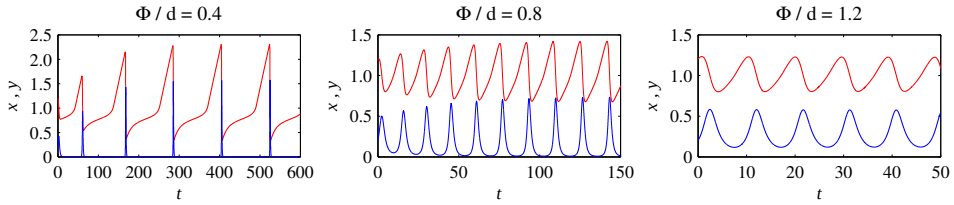

Figure 1: Solutions of Eqs. (8-10), with initial conditions $x\ (= P) = 1.2$ and $y\ (= \sqrt{E_M}) = 0.2$, $d_0 = 10^{-3}$, $d = 0.1$, $\tilde{P} = 1.05$, $\lambda = 5$, and $\frac{\Phi}{d} = 0.4,\ 0.8,\ 1.2$ as indicated above each panel. Red denotes $x = P$, blue $y = \sqrt{E_M}$.

3..2 Stochastic Model

We extend Eqs. (8)-(9) to a stochastic model by including a Gaussian white-noise ξ in Φ as $\Phi \to \Phi + \xi$, where ξ satisfies

$$\langle \xi(t)\xi(t') \rangle = 2Q_x \delta(t - t'). \tag{11}$$

Here, the angular brackets denote averages; Q_x is the amplitude of the stochastic noise ξ; $\delta(t - t')$ means that the memory time of ξ is shorter than any other characteristic time scales (e.g., ELM period) in the system. Physically, ξ represents the fluctuating energy flux of unresolved scales that are not included for the deterministic modeling, e.g., incoherent interaction, the contribution to the outward energy flux at the edge (e.g. [3, 52]), pellet pacing [53], mini-avalanches [31], etc. Letting $x \equiv P$ and $y^2 \equiv E_M$ where y is proportional to magnetic field and including another Gaussian white-noise η for the equation for y, we recast Eqs. (8)-(10) as follows:

$$\frac{dx}{dt} = \Phi - \tilde{D}(x)x - xy^2 + \xi = f + \xi, \tag{12}$$

$$\frac{dy}{dt} = \frac{1}{2}\lambda(x - 1)y + \eta = g + \eta, \tag{13}$$

$$\tilde{D} = d_0 + d(x - c^2 x^4)\Theta(\tilde{P} - x). \tag{14}$$

η in Eq. (13) is chosen to be independent of ξ, so $\langle \xi(t)\eta(t') \rangle = 0$, and to have the following property

$$\langle \eta(t)\eta(t') \rangle = 2Q_y \delta(t - t'), \tag{15}$$

where Q_y is the amplitude of η. As in the case of ξ, η includes both contributions from the internal (e.g. incoherent unresolved-scale dynamics) and any external perturbation. The absolute magnitude of Q_x and Q_y would depend very much on a particular scenario such as turbulence model and experimental conditions (plasma configurations). Our aim is thus to investigate the generic effect of stochastic noise on ELM dynamics by varying Q_x and Q_y.

Due to non-zero ξ and η, x and y no longer evolve deterministically but instead take different values around what are expected from the deterministic model. For the Langevin

model in Eqs. (11)-(15), the joint PDF $p = p(x, y, t)$ can be shown to satisfy the Fokker-Planck equation [39]

$$\frac{\partial p}{\partial t} = -\frac{\partial}{\partial x}(f\,p) - \frac{\partial}{\partial y}(g\,p) + Q_x\frac{\partial^2 p}{\partial x^2} + Q_y\frac{\partial^2 p}{\partial y^2} \equiv -\partial_x J_x - \partial_y J_y, \tag{16}$$

where

$$f \equiv \Phi - \tilde{D}(x)x - xy^2, \qquad g \equiv \frac{\lambda}{2}(x-1)y, \tag{17}$$

$$J_x = fp - Q_x\partial_x p, \qquad J_y = gp - Q_y\partial_y p. \tag{18}$$

From the joint PDF $p(x, y, t)$, the marginal PDFs are obtained as $p(x, t) = \int dy\, p(x, y, t)$ and $p(y, t) = \int dx\, p(x, y, t)$. We note that an alternative approach to the Fokker-Planck method is to perform multiple stochastic simulations of the Langevin equations. One of the advantages of the Fokker-Planck method is that a high-quality smooth PDF as well as various information diagnostics can be obtained provided that a sufficiently large number of grid points are used. However, the computational cost increases significantly as the number of variables increases. On the other hand, the alternative method of stochastic simulations requires many multiple runs for high-quality time-dependent PDFs and also needs to overcome technical challenges in data binning for constructing PDFs and the accurate calculation of information diagnostics, as discussed in [54].

4. Numerical methods

We wish to solve the Fokker-Planck equation in Eqs. (16)-(18) with the boundary conditions $p(x \to \pm\infty, y, t) = 0$ and $p(x, y \to \pm\infty, t) = 0$. As in [30, 31], the 'spatial' variables x and y are discretised via second-order finite differences, with grid spacings as small as 10^{-3} in both. The time-stepping is second-order Runge-Kutta, with time steps as small as 2×10^{-5}.

In principle calculations could be done where $\pm y$ are different, but we only consider symmetric solutions here, satisfying $p(x, y, t) = p(x, -y, t)$. Physically, this is because a similar effect on ELM dynamics is expected from magnetic fluctuations with $y > 0$ and $y < 0$, which obviously give the same magnetic fluctuation E_M. This mathematically gets translated to the symmetry condition $\frac{\partial}{\partial y}p = 0$ being imposed at $y = 0$, permitting us to restrict the computational domain $y \geq 0$ only.

The remaining computational parameters define the size of the 'box', that is, x_{min}, x_{max}, and y_{max}. These need to be adjusted so that the solution is concentrated sufficiently far away from these boundaries that such a finite box is still a good approximation to the true infinite domain. A useful check here is to track the total probability integral $\iint p(x, y, t)\, dxdy$, which should remain conserved (and equal to one) according to the Fokker-Planck equation. If the computational box was chosen to be sufficiently large (and the grid spacing also sufficiently fine), this integral was always conserved, to within 10^{-4}.

5. Results

We fix the parameters $d_0 = 10^{-3}$, $d = 0.1$, $\tilde{P} = 1.05$, and $\lambda = 5$. $\frac{\Phi}{d}$ was varied in the range $[0.4, 1.2]$. The noise level in y was fixed at $Q_y = 10^{-5}$; in x we considered the range $Q_x = 10^{-5} - 10^{-3}$. We will here present results for only $Q_x = 10^{-5}$ and 10^{-4}. The initial conditions were always Gaussian PDFs with $\langle x(0)\rangle = 1.2$, $\langle y(0)\rangle = 0.2$, $\sigma_x(0) = \sigma_y(0) = 0.04$.

5..1 Constant $\frac{\Phi}{d} = 0.4,\ 0.8,\ 1.2$

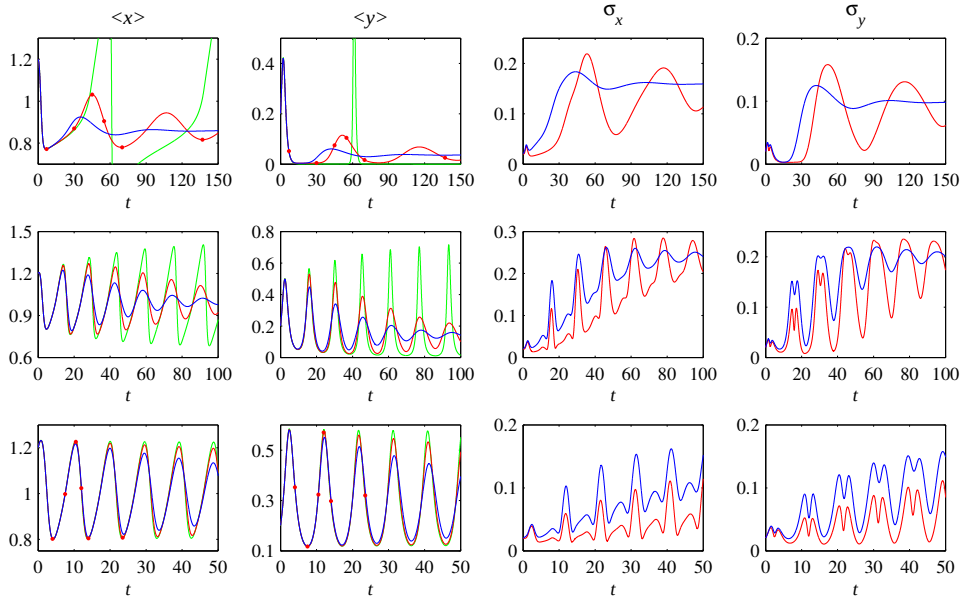

Figure 2: From left to right, the four columns show the averages $\langle x \rangle$ and $\langle y \rangle$, and the standard deviations σ_x and σ_y, as labeled above each column. The top row is $\frac{\Phi}{d} = 0.4$, the middle row $\frac{\Phi}{d} = 0.8$, and the bottom row $\frac{\Phi}{d} = 1.2$. Within each panel red is $Q_x = 10^{-5}$, and blue is $Q_x = 10^{-4}$. The green curves for $\langle x \rangle$ and $\langle y \rangle$ show the noise-less ODE results from Figure 1.

Figure 2 shows the most basic diagnostics $\langle x \rangle$, $\langle y \rangle$, σ_x and σ_y, and how they vary with Q_x and Φ. For all Φ values, the collapse of $\langle x \rangle$ is followed by the sudden increase in fluctuations σ_x and σ_y in addition to $\langle y \rangle$. This is because y is driven by x while evolving linearly with respect to y. For the largest value $\frac{\Phi}{d} = 1.2$, we see that $\langle x \rangle$ and $\langle y \rangle$ match the original ODE extremely well, with the only difference being that the ODE settles in to a periodic solution, whereas the stochastic model exhibits very gradually decaying oscillations until it settles into a stationary PDF after a sufficiently long time. We will consider the meaning of this decay in a moment, but first we consider the smaller Φ values. For $\frac{\Phi}{d} = 0.8$ the situation is similar as before, except that now the oscillations in the stochastic model decay more rapidly.

For the smallest value $\frac{\Phi}{d} = 0.4$ though, the mean value from the Fokker-Planck equation only agrees with the original ODE model up to around $t \approx 30$, which is well before the ODE has its first 'burst'. The stochastic model still exhibits (decaying) oscillations in mean values, but not as extreme as the bursts in the ODE. This discrepancy arises from how small y can become in the ODE versus the Fokker-Planck model. In the first panel of Figure 1 y reaches values smaller than 10^{-20} in between the bursts, and it is precisely these extremely small values that make the bursts so explosive. In contrast, in the Fokker-Planck model, stochastic noise ($Q_x, Q_y \neq 0$) prevents $\langle y \rangle$ from becoming smaller than ~ 0.01, which then causes the bursts to be far less explosive. Physically, this is similar to the degradation of electron heat transport due to stochastic magnetic fields [55]. In our model, due to the coupling of x and y, the increase in stochastic noise in x (larger Q_x) for the fixed Q_y induces stronger stochastic magnetic field y. Thus, the larger Q_y, Q_x are, the less explosive the bursts would be and the more quickly the oscillations would disappear. For instance, for $Q_x = 10^{-4}$, oscillations

disappear more quickly compared with the case of $Q_x = 10^{-5}$ for the same Q_y, reminiscent of ELM suppression for a sufficiently larger resonant stochastic magnetic perturbation [36, 56].

In addition to ELM suppression noted above, it is of interest that our results show the signature of ELM mitigation in the early evolution stage where the oscillation frequency tends to increase more for larger Q_x. Specifically, in Figure 2, the local maxima of $\langle y \rangle$ for $\Phi/d = 0.4$ occur around $t \sim 40, 50, 60$ (in blue, red, green) for $Q_x = 10^{-4}, 10^{-5}, 0$, respectively, indicating the initial faster oscillations for larger Q_x. This demonstrates that extreme bursts of giant ELMs can be mitigated by stochastic noises in fusion devices as they are turned into smaller and higher frequency ELMs, followed by the ELM suppression. Overall, in all cases of $Q_x, \Phi/d$, the larger the stochastic noise is, the less prominent ELMs become.

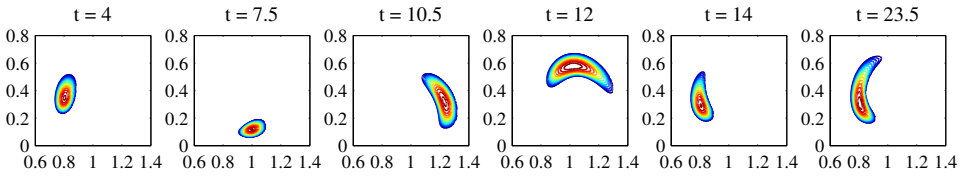

Figure 3: Contours of the $\frac{\Phi}{d} = 1.2$, $Q_x = 10^{-5}$ PDFs $p(x, y, t)$, at the six times indicated above each panel. The horizontal and vertical axes correspond to x and y, respectively, but are not labelled to allow more space for the actual PDFs. Contours are on a logarithmic scale, with the smallest value (in blue) being 0.01, and then doubling for every further contour level toward the maximum in red.

To understand the meaning of the gradually decaying oscillations in $\langle x \rangle$ and $\langle y \rangle$ seen in Figure 2, we must examine the shape of the PDFs, and how it evolves in time. Figure 3 shows these results for $\frac{\Phi}{d} = 1.2$ — which we recall was the most straightforward case in Figure 2 — at the six times $t = 4,\ 7.5,\ 10.5,\ 12,\ 14,\ 23.5$. The significance of these particular times is indicated by the red dots in the $\langle x \rangle$ and $\langle y \rangle$ panels in the bottom row of Figure 2: $t = 4$ is when $\langle x \rangle$ has its first minimum, $t = 10.5$ is the maximum after that, $t = 14$ is the next minimum, and finally $t = 23.5$ is the next minimum again, after one full cycle. Correspondingly also, $t = 7.5$ is the first minimum in $\langle y \rangle$, and $t = 12$ is the maximum after that.

And sure enough, if we consider the first five panels in Figure 3, we see the PDF swirling once around the loop that constitutes the ODE trajectory in the x-y-plane. If we next compare the final two panels, at $t = 14$ and 23.5, we see that the PDF is indeed located at exactly the same position, since $t = 23.5$ was chosen because it is one further loop around the trajectory. We note though that the PDF at $t = 23.5$ is somewhat more spread out around the loop than the PDF at $t = 14$. That is, the presence of noise is causing the system to gradually 'forget' its particular phase along the ODE trajectory. The PDF spreading can thus be viewed as a type of phase-mixing. We can then already guess as to what the final equilibrated PDF will look like; it should be uniformly spread out along the loop, with all knowledge of any particular phase along the ODE trajectory having been erased by the presence of noise. At that point of course the averages $\langle x \rangle$ and $\langle y \rangle$ would equilibrate at roughly the centre of the loop. The gradually decaying oscillations in Figure 2 due to phase-mixing initiates the adjustment to the final equilibrated PDFs.

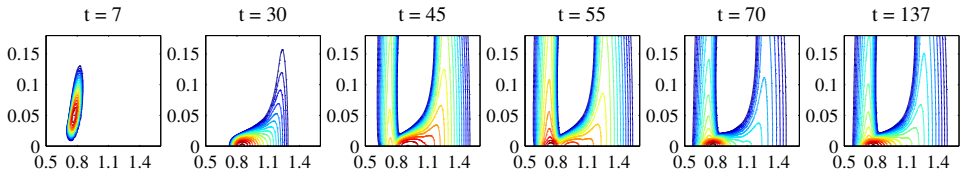

Figure 4: As in Figure 3, but now for $\frac{\Phi}{d} = 0.4$.

Figure 4 shows how the PDF evolves in time for $\frac{\Phi}{d} = 0.4$, again showing particular times corresponding to maxima/minima of $\langle x \rangle$, as seen in the red dots in the top-left panel in Figure 2. Even at times when $\langle y \rangle$ is supposedly large, the PDFs are still concentrated toward $y = 0$ far more than in Figure 3, making the behaviour less clear, even after focusing on very small y by showing only a small part of the whole computational box. The behaviour corresponding to maxima/minima in $\langle x \rangle$ is recognisable though. Also, comparing the final two panels, at $t = 70$ and 137, which again correspond to successive minima in $\langle x \rangle$, we can see that the peak position is again in the same place, and the PDF at the later time is again somewhat more spread out than at the earlier time, indicative of this gradual spreading-out around the entire loop.

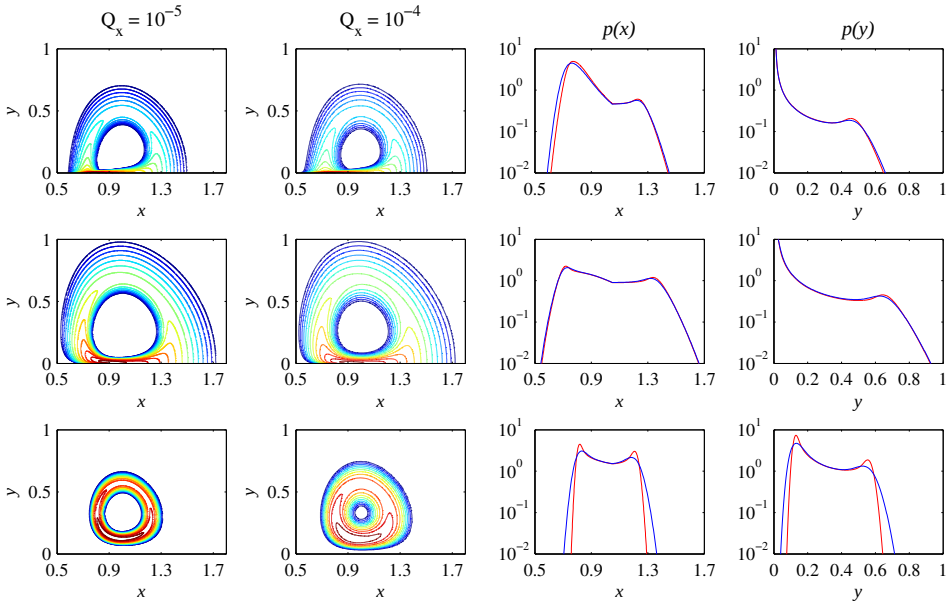

Figure 5: The first two columns show the equilibrated PDFs $p(x, y)$ for $Q_x = 10^{-5}$ and 10^{-4}, as indicated above the columns. The contour intervals are as in Figures 3 and 4, so starting at 0.01 in blue and then doubling with every further contour toward the maxima in red. The third column shows the marginal $p(x)$, and the fourth column the marginal $p(y)$. For these marginal PDFs red is $Q_x = 10^{-5}$ and blue is $Q_x = 10^{-4}$. The top row is $\frac{\Phi}{d} = 0.4$, the middle row is $\frac{\Phi}{d} = 0.8$, and the bottom row is $\frac{\Phi}{d} = 1.2$.

Figure 5 shows the final stationary PDFs after all the oscillations in Figure 2 have decayed away in the long time $t \to \infty$ limit. Interestingly, they form loops around the original ODE trajectories. That is, the final PDFs 'know' that the system must be somewhere close to the

ODE trajectories, but the presence of noise together with the large time limit have erased all knowledge of the phase along the trajectory. The comparison between the two Q_x values corroborates this: larger Q_x broadens the thickness of the track around the ODE trajectory. In the limit $Q_x \to 0$, this thickness would collapse to zero, and these PDFs would smoothly tend to the ODE trajectories.

Turning next to the third and fourth columns in Figure 5, these show the marginal PDFs $p(x)$ and $p(y)$. We note first that they are both bimodal[3], for all combinations of Φ and Q_x, a local minimum forming around $x = 1$ (instability boundary). Next, $p(y)$ peaks at $y = 0$ for $\frac{\Phi}{d} = 0.4$ and 0.8, but at $y > 0$ for $\frac{\Phi}{d} = 1.2$. Both bimodal $p(x)$ and $p(y)$ are more symmetric for larger Φ. One final point to note here is how the two Q_x values yield almost identical results for $\frac{\Phi}{d} = 0.4$ and 0.8, whereas for $\frac{\Phi}{d} = 1.2$ both $p(x)$ and $p(y)$ drop off more rapidly at the edges for $Q_x = 10^{-5}$ than for $Q_x = 10^{-4}$ (as one might expect).

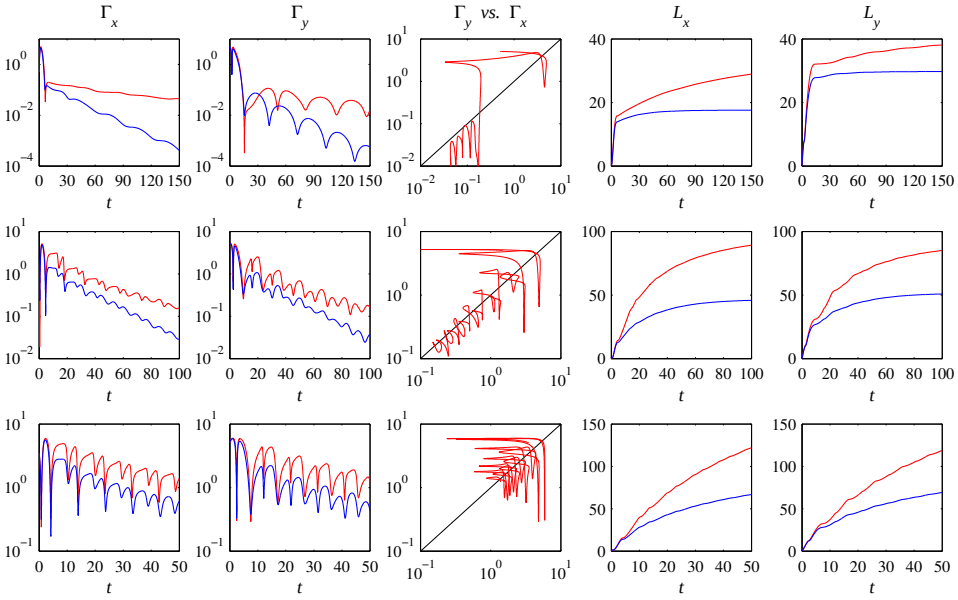

Figure 6: As labeled above them, the first two columns show Γ_x and Γ_y as functions of time, with red being $Q_x = 10^{-5}$ and blue $Q_x = 10^{-4}$. The third column replots the red ($Q_x = 10^{-5}$) data as a curve in the (Γ_x, Γ_y)-plane, with the diagonal line corresponding to $\Gamma_x = \Gamma_y$. The final two columns show the corresponding $\mathcal{L}_x$ and $\mathcal{L}_y$. As before in Figure 2, the top row is $\frac{\Phi}{d} = 0.4$, the middle row $\frac{\Phi}{d} = 0.8$, and the bottom row $\frac{\Phi}{d} = 1.2$.

A useful information geometric method to quantify the time-evolution of PDFs in Figures 3-4 is the information rate Γ_x, Γ_y in Eq. (7) and information length $\mathcal{L}_x, \mathcal{L}_y$ in Eq. (6), shown in Figure 6. As before in Figure 2, the top row is $\frac{\Phi}{d} = 0.4$, the middle row $\frac{\Phi}{d} = 0.8$, and the bottom row $\frac{\Phi}{d} = 1.2$. In the first two columns, Γ_x and Γ_y are shown as functions of time for $Q_x = 10^{-5}$ (in red) and blue $Q_x = 10^{-4}$ (in blue). For all Φ's, the overall amplitude of Γ_x and Γ_y decrease over time due to the stochastic noises and phase-mixing, discussed above. It is entertaining to see that Γ_x and Γ_y oscillate out of phase and cross

[3]Note that bimodal PDFs here can be due to long-time spent around the inflection points of oscillations and can also result from sinusoidal signals.

each other occasionally, manifesting the information-geometric self-regulatory oscillations. Alternatively, recalling that Γ_x and Γ_y quantify how quickly the information changes in $p(x,t)$ and $p(y,t)$, respectively, these oscillations signify the self-regulation of information change.

To see this more clearly, the third column shows the information portrait, where the red ($Q_x = 10^{-5}$) data are plotted as a red curve in the (Γ_x, Γ_y)-plane, together with the diagonal line $\Gamma_x = \Gamma_y$ in black. Along the diagonal line $\Gamma_x = \Gamma_y$, the time-scales of the information change in x and y match. When $\Gamma_x > \Gamma_y$, x dominates y, while for $\Gamma_x < \Gamma_y$, y dominates x. Thus, the oscillations of Γ_x and Γ_y around this diagonal line in Figure 6 manifest the competition of the time scales of the information change in x and y. Interestingly, for $\frac{\Phi}{d} = 1.2$ in the bottom row, Γ_x and Γ_y look quite symmetric around $\Gamma_x = \Gamma_y$, suggesting high-correlation and self-regulation. The information portraits become less symmetric for $\frac{\Phi}{d} = 0.8, 0.4$ due to larger bursts and initial transients.

The final two columns show the corresponding $\mathcal{L}_x$ and $\mathcal{L}_y$ for $Q_x = 10^{-5}$ (in red) and blue $Q_x = 10^{-4}$ (in blue). $\mathcal{L}_x$ and $\mathcal{L}_y$ increase in time due to non-zero Γ_x and Γ_y (see Eq. (6)), respectively, towards their asymptotic values (as $t \to \infty$). For all Φ's, the overall time-evolutions of $\mathcal{L}_x$ and $\mathcal{L}_y$ are similar qualitatively. Quantitatively, $\mathcal{L}_y$ is larger than $\mathcal{L}_x$ for $\Phi/d = 0.4$ due to a large contribution to Γ_y from a narrow PDF $p(y,t)$ (small σ_y) around $t \sim 10 - 30$ (e.g., see Figure 2). We recall that Γ_y roughly measures the change in a PDF relative to its width σ_y (the uncertainty). As Φ/d increases, y no longer forms such a narrow PDF near $y = 0$, and x and y are more strongly correlated exhibiting similar behaviour (with some phase shift), leading to more similar values $\mathcal{L}_x$ and $\mathcal{L}_y$. These results thus suggest that the strong correlation between x and y through self-regulation can be inferred from the competition between Γ_x and Γ_y [30, 31] or similar behaviour of $\mathcal{L}_x$ and $\mathcal{L}_y$ [47].

5..2 Time-dependent Φ: Forward and backward processes

Obtaining a stationary PDF requires a sufficiently long time[4] and may not be realised in real systems when some model parameters change on shorter time scales. It is thus of interest to investigate the ELM dynamics for time-dependent parameters. As an example, we consider i) the forward process of a 'jump-up' case where the input power Φ jumps discretely every 10 time units taking the values $\frac{\Phi}{d} = [0.4, 0.6, 0.8, 1.0, 1.2]$; and ii) the backward process of a 'jump-down' case where Φ jumps down every 10 time units with $\frac{\Phi}{d} = [1.2, 1.0, 0.8, 0.6, 0.4]$. Here, we choose Φ to be symmetric under time-reversal to explore the possibility of hysteresis where the forward and backward dynamics are not time reversible.

Results are shown in Figures 7-8, following the same conventions as in Figures 2 and 6, respectively. The top and bottom rows are for the 'jump-up' and 'jump-down' cases, respectively. Again, red and blue are for $Q_x = 10^{-5}$ and $Q_x = 10^{-4}$, respectively.

In Figure 7, the four columns show $\langle x \rangle$, $\langle y \rangle$, σ_x, and σ_y, as labeled above each column. For the jump-up and jump-down cases, the oscillation periods of $\langle x \rangle$ and $\langle y \rangle$, respectively increase and decrease with time, as expected from smaller periods for larger Φ. Within the total 50 time units, the total number of oscillations is however larger for the jump-down case than for the jump-up case. This means that the jump-down case should be run further to a smaller Φ value if we wanted to recover the (longer) period oscillation similar to that

[4]This would be of $O(10^4)$ time units for $\frac{\Phi}{d} = 0.4$ and $Q_x = Q_y = 10^{-5}$, corresponding to $O(10 - 100)$ msecs. It will be even longer for smaller Q_x, Q_y.

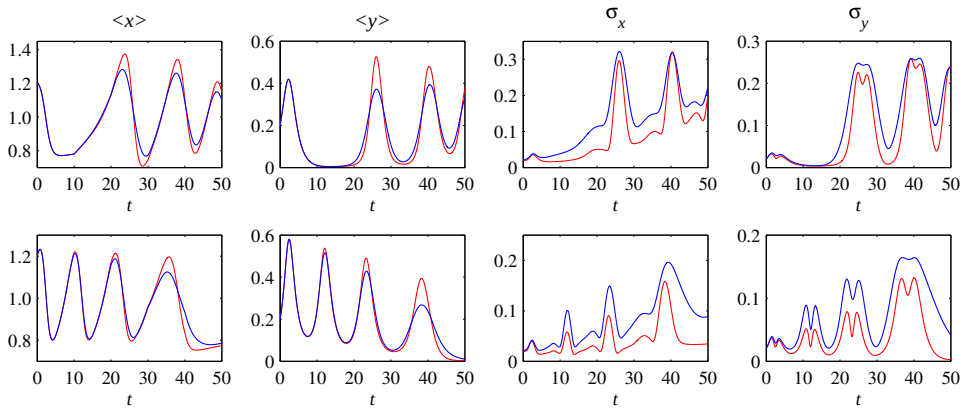

Figure 7: As in Figure 2, the four columns show the averages $\langle x \rangle$ and $\langle y \rangle$, and the standard deviations σ_x and σ_y, as labeled above each column. The top row is the 'jump-up' case $\frac{\Phi}{d} = [0.4, 0.6, 0.8, 1.0, 1.2]$, and the bottom row the 'jump-down' case $\Phi = [1.2, 1.0, 0.8, 0.6, 0.4]$. Within each panel red is $Q_x = 10^{-5}$, and blue is $Q_x = 10^{-4}$.

at the beginning of the jump-up case.[5] Furthermore, the overall amplitude of σ_x and σ_y is smaller for the jump-down than for the jump-up, suggesting stronger fluctuations in the jump-up. These are indications of hysteresis, manifested by the asymmetry between forward and backward processes.

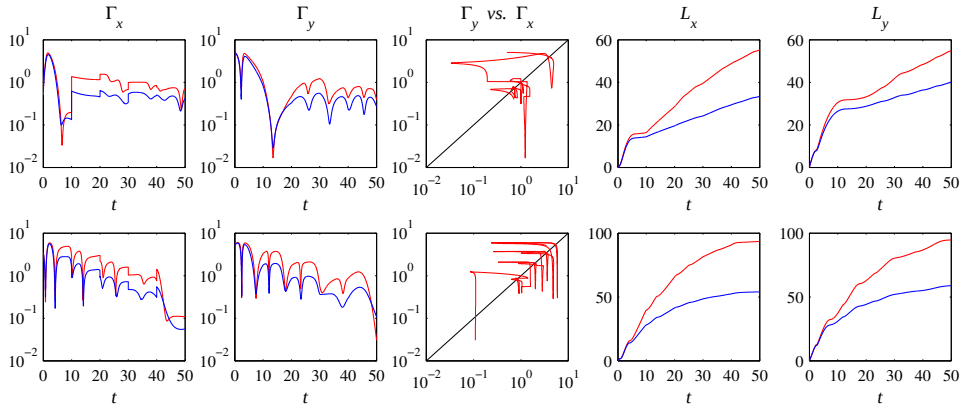

Figure 8: As in Figure 6, the first two columns show Γ_x and Γ_y as functions of time, with red being $Q_x = 10^{-5}$ and blue $Q_x = 10^{-4}$. The third column replots the red ($Q_x = 10^{-5}$) data as a curve in the (Γ_x, Γ_y)-plane, with the diagonal line corresponding to $\Gamma_x = \Gamma_y$. The final two columns show the corresponding $\mathcal{L}_x$ and $\mathcal{L}_y$. As in Figure 7, the top row is the 'jump-up' case, and the bottom row the 'jump-down' case.

Hysteresis is also inferred from Figure 8 with differences between the forward and backward processes in the overall time-evolution of path-dependent information geometric diagnostics – the information rates Γ_x and Γ_y, and information lengths $\mathcal{L}_x$ and $\mathcal{L}_y$. In particular, self-regulatory oscillations are more clearly manifested for the backward process where Γ_x

[5]This can be viewed as a lower threshold Φ for the backward process.

and Γ_y exhibit more crossings around $\Gamma_x = \Gamma_y$, leading to more similar evolution of $\mathcal{L}_x$ and $\mathcal{L}_y$. In comparison with the forward process, the backward process proceeds with smaller values of σ_x and σ_y (weaker fluctuations), as noted above. This then leads to larger values of $\mathcal{L}_x$ and $\mathcal{L}_y$ for the backward process compared with the forward process since $\mathcal{L}_x$ and $\mathcal{L}_y$ are the information geometric (dimensionless) distance measuring roughly the total change in a PDF relative to the standard deviation. Finally, it is interesting that Γ_x suddenly increases (decreases) every ten time units for the forward (backward) process when Φ jumps up (down). This demonstrates that the information rate is sensitive to changes in the system [37, 43].

6. Conclusions

We proposed and investigated a stochastic ELM model in the limit where the poloidal flows are negligible compared to the pressure gradient by using time-dependent PDF and path-dependent information geometry analysis. We calculated the exact time-dependent PDFs of pressure gradient and magnetic fluctuation amplitude by numerically solving the Fokker-Planck equation for different input energy fluxes and stochastic noise amplitudes. Stochastic noises were shown to introduce phase-mixing by mixing different random trajectories, with a dramatic effect on mitigating large ELMs with a slight increase in ELM frequency for a small input power $\Phi/d = 0.4$ in the initial evolution, reminiscent of the ELM mitigation by magnetic perturbation or pellet injections[35, 36, 57], followed by oscillation (ELM) suppression [56].

For larger $\Phi/d = 0.8, 1.2$, stochastic noise mainly reduced the oscillation amplitude without much effect on oscillation frequency, indicative of ELM suppression. The ELM suppression could be due to the stabilisation of the pressure profile by stochastic noise (e.g., as stochastic magnetic field increases transport, reducing the pressure gradient [55]). A more detailed study on the effect of stochastic noise strength on the frequency and amplitude of ELMs as well as the bifurcation from ELM mitigation to suppression for a sufficiently large stochastic noise [56] is left for future work.

From the exact time-dependent PDFs, we calculated the path-dependent information rate and information length and showed that the self-regulation of the pressure gradient and magnetic fluctuations are manifested by the competition of their information rates (e.g. as oscillations about $\Gamma_x = \Gamma_y$ in the information portrait) while the sudden change to the system is reflected in an abrupt change in the information rate. Furthermore, for time-dependent energy fluxes, we compared the results for the forward and backward processes where the energy flux increased and decreased, respectively, in discrete jumps, highlighting hysteresis not only in usual physical variables but also in information geometry.

While the results in this paper are limited to the case without poloidal flows, the effects of stochastic noises as well as self-regulatory information geometry are likely to be similar in fuller models. Obtaining high-resolution time-dependent PDFs for ELMs including the effect of poloidal flows requires considerably more expensive computational resources and time and will be left for future work. Finally, we note that our methods can in principle be applied for the analysis of data from other turbulence models [46, 48] or observational data [58, 59] from experiments by sampling different (temporal and/or spatial) selections of data, for instance, using moving-time windows.

Author Contributions: EK conceived of and designed the study; RH developed the code and performed simulations. EK and RH investigated results and wrote/approved the manuscript.

The authors declare that they have no competing interests.

We thank Dr Yasmin Andrew for helpful discussions.

References

[1] B. Kadomtsev and E.W. Laing, *Tokamak Plasma: A Complex Physical System* (IOP Pub. Ltd, 1992).

[2] C. Hildago, M.A. Pedrosa, and B. Goncalves, Fluctuations, sheared radial electric fields and transport interplay in fusion plasmas, New J. Phys. **4**, 51 (2002).

[3] Y. Sarazin and P. Ghendrih, Intermittent particle transport in two-dimensional edge turbulence, Phys. Plasmas **5**, 4214 (1998).

[4] K. Itoh, S.-I. Itoh, A. Fukuyama, and M. Yagi, Theory of plasma turbulence and structural formation – nonlinearity and statistical view, J. Plasma Fusion Res. **79**, 608 (2003).

[5] F. Wagner, G. Becker, K. Behringer, D. Campbell, A. Eberhagen, W. Engelhardt, G. Fussmann, O. Gehre, J. Gernhardt, G. von Gierke *et al.*, Regime of improved confinement and high-beta in neutral-beam-heated divertor discharges of the ASDEX tokamak, Phys. Rev. Lett. **49**, 1408-1412 (1982).

[6] P.H. Diamond, S.-I. Itoh, K. Itoh, and T.S. Hahm, Zonal flows in plasma – a review, Plasma Phys. Contr. Fusion **47**, R35 (2005).

[7] C.S. Chang, S. Ku, G.R. Tynan, R. Hager, R.M. Churchill, I. Cziegler, M. Greenwald, A.E. Hubbard, and J.W. Hughes, Fast low-to-high confinement mode bifurcation dynamics in a tokamak edge plasma gyrokinetic simulation, Phys. Rev. Lett. **118**, 175001 (2017).

[8] L. Schmitz, The role of turbulence-flow interactions in L- to H-mode transition dynamics: recent progress, Nuclear Fusion **57**, 025003 (2017).

[9] E. Kim and P.H. Diamond, Zonal flows and transient dynamics of the L-H transition, Phys. Rev. Lett. **90**, 185006 (2003).

[10] M.A. Malkov and P.H. Diamond, Weak hysteresis in a simplified model of the L-H transition, Phys. Plasmas **16**, 012504 (2009).

[11] H. Zhu, S.C. Chapman, and R.O. Dendy, Robustness of predator-prey models for confinement regime transitions in fusion plasmas, Phys. Plasmas **20**, 042302 (2013).

[12] C.F. Maggi, E. Delabie, T.M. Biewer, M. Groth, N.C. Hawkes, M. Lehnen, E. de la Luna, K. McCormick, C. Reux, F. Rimini *et al.*, L-H power threshold studies in JET with Be/W and C wall, Nuclear Fusion **54**, 023007 (2014).

[13] Y. Andrew, J.-P. Bähner, R. Battle, and T. Jirman, H-mode power threshold studies on MAST, Plasma **2**, 328 (2019).

[14] L. Schmitz et al., Role of zonal flow predator-prey oscillations in triggering the transition to H-mode confinement, Phys. Rev. Lett. **108**, 155002 (2012).

[15] T. Kobayashi, K. Itoh, T. Ido, K. Kamiya, S.-I. Itoh, Y. Miura, Y. Nagashima, A. Fujisawa, S. Inagaki, K. Ida, and K. Hoshino, Spatiotemporal structures of edge limit-cycle oscillation before L-to-H transition in the JFT-2M tokamak, Phys. Rev. Lett. **111**, 035002 (2013).

[16] J. Cheng, Q. Dong, K. Itoh, L.W. Yan, M. Xu, K.J. Zhao, W.Y. Hong, Z.H. Huang, X.Q. Ji, W.L. Zhong *et al.*, Dynamics of low-intermediate-high-confinement transitions in toroidal plasmas, Phys. Rev. Lett. **110**, 265002 (2013).

[17] G.S. Xu, H.Q. Wang, M. Xu, B.N. Wan, H.Y. Guo, P.H. Diamond, G. R. Tynan, R. Chen, N. Yan, D.F. Kong *et al.*, Dynamics of L-H transition and I-phase in EAST, Nuclear Fusion **54**, 103002 (2014).

[18] Z. Yan, G.R. McKee, R. Fonck, P. Gohil, R.J. Groebner, and T.H. Osborne, Observation of the L-H confinement bifurcation triggered by a turbulence-driven shear flow in a tokamak plasma, Phys. Rev. Lett. **112**, 125002 (2014).

[19] J.J. Rasmussen, A.H. Nielsen, J. Madsen, V. Naulin, and G.S. Xu, Numerical modeling of the transition from low to high confinement in magnetically confined plasma, Plasma Phys. Contr. Fusion **58**, 014031 (2016).

[20] T.I. Wagner, The history of research into improved confinement regimes, Europ. Phys. J. H **43**, 523 (2018).

[21] K. Burrell, Effects of $E \times B$ velocity shear and magnetic shear on turbulence and transport in magnetic confinement devices, Phys. Plasmas **4**, 1499, (1997).

[22] T.S. Hahm, Physics behind transport barrier theory and simulations, Plasma Phys. Control. Fusion **44**, A87 (2002).

[23] M.G. Shats, H. Xia, and H. Punzmann, Suppression of turbulence by self-generated and imposed mean flows, Phys. Rev. Lett. **99**, 164502 (2007).

[24] E. Kim and I. Movahedi, Effect of enhanced dissipation by shear flows on transient relaxation and probability density function in two dimensions, Phys. Plasmas **24**, 112306 (2017).

[25] E. Kim, Consistent theory of turbulent transport in two-dimensional magnetohydrodynamics, Phys. Rev. Lett. **96**, 084504 (2006).

[26] G. Tynan *et al.*, Recent progress towards a physics-based understanding of the H-mode transition, Plasma Phys. Control. Fusion **58**, 044003 (2016).

[27] L. Schmitz, L. Zeng, T.L. Rhodes, J.C. Hillesheim, W.A. Peebles, R.J. Groebner, K.H. Burrell, G.R. McKee, Z. Yan, G.R. Tynan, P.H. Diamond, J.A. Boedo, E.J. Doyle, B.A. Grierson, C. Chrystal, M.E. Austin, W.M. Solomon, and G. Wang, The role of zonal flows and predatorprey oscillations in triggering the formation of edge and core transport barriers, Nuclear Fusion **54**, 073012 (2014).

[28] M. Dam, M. Brons, J.J. Rasmussen, V. Naulin, and G.S. Xu, Bifurcation analysis and dimension reduction of a predator-prey model for the L-H transition, Phys. Plasmas **20**, 102302 (2013).

[29] P. Gohil, T.E. Evans, M.E. Fenstermacher, J.R. Ferron, T.H. Osborne, J.M. Park, O. Schmitz, J.T. Scoville, and E.A. Unterberg, LH transition studies on DIII-D to determine H-mode access for operational scenarios in ITER, Nuclear Fusion **51**, 103020 (2011).

[30] E. Kim and R. Hollerbach, Time-dependent probability density functions and information geometry of the low-to-high confinement transition in fusion plasma, Phys. Rev. Res. **2**, 023077 (2020).

[31] R. Hollerbach, E. Kim, and L. Schmitz, Time-dependent probability density functions and information diagnostics in forward and backward processes in a stochastic prey-predator model of fusion plasmas. Phys. Plasmas **27**, 102301 (2020).

[32] V.B. Lebedev, P.H. Diamond, I. Gruzinov, and B.A. Carreras, A minimal dynamical model of edge localized mode phenomena, Phys. Plasmas **2**, 3345 (1995).

[33] M. Kim, H.K. Park, J. Lee, G.S. Yun, X.Q. Xu, and M. Bécoulet, BOUT++ nonlinear simulation for a comparative study with the measured 2D ELM structures in the KSTAR H-mode plasma, Phys. Plasmas **26**, 052502 (2019).

[34] Y.M. Wang, X.Q. Xu, Z. Yan, G.R. Mckee, B.A. Grierson, T.Y. Xia, and X. Gao, Simulation of density fluctuations before the L-H transition for hydrogen and deuterium plasmas in the DIII-D tokamak using the BOUT++ code, Nuclear Fusion **58**, 026026 (2018).

[35] A.W. Leonard, Edge-localized-modes in tokamaks, Phys. Plasmas **21**, 090501 (2014).

[36] F. Orain, M. Hoelzl, F. Mink, M. Willensdorfer, M. Bécoulet, M. Dunne, S. Günter, G. Huijsmans, K. Lackner, S. Pamela, W. Suttrop, E. Viezzer, ASDEX Upgrade Team, and EUROfusion MST Team, Non-linear modeling of the threshold between ELM mitigation and ELM suppression by resonant magnetic perturbations in ASDEX upgrade, Phys. Plasmas **26**, 042503 (2019).

[37] E. Kim, Information geometry, fluctuations, non-equilibrium thermodynamics, and geodesics in complex systems, Entropy **23**, 1393 (2021).

[38] G.Y. Park *et al.*, Flux-driven simulations of turbulence collapse, Phys. Plasmas **22**, 032505 (2015).

[39] H. Risken, *The Fokker-Planck Equation: Methods of Solutions and Applications* (Springer, 2013).

[40] A.M. Kowalski et al., Distances in probability space and the statistical complexity setup, Entropy **13**, 1055 (2011).

[41] T. Parr, L. Da Costa, and K.J. Friston, Markov blankets, information geometry and stochastic thermodynamics, Phil. Trans. Roy. Soc. A **378**, 20190159 (2019).

[42] M. Oizumi, N. Tsuchiya, and S. Amari, Unified framework for information integration based on information geometry, Proc. Nat. Acad. Sci. **113**, 14817 (2016).

[43] A.J. Guel-Cortez and E. Kim, Information geometric theory in the prediction of abrupt changes in system dynamics, Entropy **23**, 694 (2021).

[44] E. Kim and R. Hollerbach, Geometric structure and information change in phase transitions, Phys. Rev. E **95**, 062107 (2017).

[45] E. Kim, Q. Jacquet, and R. Hollerbach, Information geometry in a reduced model of self-organised shear flows without the uniform coloured noise approximation, J. Stat. Mech., 023204 (2019).

[46] J. Anderson, E. Kim, B. Hnat, and T. Rafiq, Elucidating plasma dynamics in Hasegawa-Wakatani turbulence by information geometry, Phys. Plasmas **27**, 022307 (2020).

[47] J. Heseltine and E. Kim, Comparing information metrics for a coupled Ornstein-Uhlenbeck process, Entropy **21**, 775 (2019).

[48] E. Kim, J. Heseltine, and H. Liu, Information length as a useful index to understand variability in the global circulation, Mathematics **8**, 299 (2020).

[49] E. Kim, Investigating information geometry in classical and quantum systems through information length, Entropy **20**, 574 (2018).

[50] N. Walkden, F. Riva, J. Harrison, F. Militello, T. Farley, J. Omotani, and B. Lipschultz, The physics of turbulence localised to the tokamak divertor volume, Comm. Phys. **5**, 139 (2022).

[51] T.L. Rhodes *et al.*, Turbulent radial correlation length in the DIII-D tokamak, United States. https://www.osti.gov/servlets/purl/766721 (2000).

[52] H.Y.W. Tsui *et al.*, A comparison of edge turbulence in tokamaks, stellarators, and reversed-field pinches, Phys. Fluids B **5**, 2491 (1993).

[53] P.T. Lang *et al.*, ELM triggering by local pellet perturbations in type-I ELMy H-mode plasma at JET, Nuclear Fusion **47**, 754 (2007).

[54] A.A. Thiruthummal and E. Kim, Monte Carlo Simulation of Stochastic Differential Equation to Study Information Geometry, in preparation (2022).

[55] A.B. Rechester and M.N. Rosenbluth, Electron heat transport in a tokamak with destroyed magnetic surfaces, Phys. Rev. Lett. **40**, 38 (1978).

[56] Y. Sun *et al.*, Nonlinear transition from mitigation to suppression of the edge localized mode with resonant magnetic perturbations in the EAST tokamak, Phys. Rev. Lett. **117**, 115001 (2016).

[57] V. Parail *et al.*, Theoretical analysis and predictive modelling of ELMs mitigation by enhanced toroidal ripple and ergodic magnetic field, IAEA: N. p., 2006. Web.

[58] H.R. Chamorro, A. Guel-Cortez, E. Kim *et al.*, Information length quantification and forecasting of power systems kinetic energy, IEEE Transactions on Power Systems, doi: 10.1109/TPWRS.2022.3146314 (2022).

[59] Y. Andrew, E. Kim, D. Kologi, L. Schmitz, and Z. Wei, Time-dependent PDF analysis of DIII-D L-H transition, Royal Society Scientific meeting – H-mode Transition and Pedestal Studies in Fusion, poster (2022).